Electronic Supplementary Material (ESI) for Journal of Materials Chemistry C.

Supplementary Information – Defect formation in chemically reduced congruent LiTaO$_3$: *ab initio* simulations and inelastic neutron scattering

Thomas Köhler,*[a] Matthias Zschornak,*[ab] Mohamed Zbiri,[c] Juliane Hanzig,[a] Christian Röder,[d] Claudia Funke,[a] Hartmut Stöcker,[a] Erik Mehner,[a] and Dirk C. Meyer[a]

S1 *In situ* INS studies on as-grown and thermally reduced C-LiTaO$_3$

The chosen samples were investigated *in situ* at different temperatures. The aim was to identify the paraelectric phase and the dynamics of defect formation. The separation of both effects is difficult, since *ab initio* simulations show that the differences between the vacancy models of $\mathrm{V}_\mathrm{O}^{\bullet\bullet}$ and V_Li' are marginal compared to the paraelectric structure.

Fig. S1 shows the *in situ* temperature treatment of as-grown (a, b) and chemically reduced (c, d) C-LiTaO$_3$, respectively. The difference is always shown as higher temperature minus lower temperature. From (a) it is clear that the dominant spectral changes are due to the phase transition into the $R\bar{3}cH$ space group. From the comparison of paraelectric and ferroelectric phase we assign this to the significant difference peaks at 5.9, 7.3, 8.5, 11.1, 13.8, 15.6, 16.7, 19.2, and 24.3 THz. These artefacts also dominate in the $\Delta g^{(n)}$ of the chemically reduced material. Additionally, the chemically reduced material shows deviations at 12.2, 13.0, 18.1, and 24.5 THz. These are attributed to the formation of vacancies in the material (see also difference curve in Fig. 8 b). In particular, if we look at the comparison between 1274 K and 924 K, we can observe difference peaks that are slightly more intense in the reduced material than in the as-grown state. However, these peaks appear in both materials and can be attributed to the defect incorporation caused by the *in situ* conditions: 6.8, 8.7, 10.6 ... 11.6 THz. Above T_C, the structural phase transition should be complete and no domain structure should be present. Therefore, a defect formation dynamic can be assumed here. The mode changes above 20 THz are difficult to identify in the high-temperature measurements due to the DEBYE-WALLER broadening and the increase in anharmonic effects[1].

S2 RAMAN studies on chemically reduced C-LiTaO$_3$

The RAMAN spectra of the investigated powders scatter in their mode intensities, which is due to the coarse powder preparation. To obtain reliable intensities, we use single crystals for RS of C-LiTaO$_3$, which were treated in a comparable way to the powders used for INS measurements. In the case of the C-LiTaO$_3$ single crystals, we find dominant spectral changes for all sample orientations when using 180° backscattering geometry. These dominant changes cannot be attributed to the stoichiometry change due to defect incorporation, but to the formation of ferroelectric domains and the associated strain fields. In order to investigate the influence of the domains and the corresponding strain in the $z(x,\mathrm{u})\bar{z}$ scattering geometry, the laser focus position was varied on the confocal microscope (see Fig. S2 a).

From the comparison of the as-grown material with the chemically reduced crystal (see Fig. 6 a), it has been shown that the intensity of A_1 and E modes are influenced by the formation of the domain structure. From Fig. S2 a it is obvious that not all of the varying modes show a depth dependence. The comparison of the spectra of the reduced material shows that especially the A_1(3LO), A_1(4LO) and E(8TO) phonon modes decrease or increase with the shift of the focus to 30 µm into the bulk material. The dependence of A_1(2LO) is weak compared to the other A_1 phonon modes. In the macroscopic description[2] the scattering process at domain walls leads to phonons that propagate at an angle to the domain wall planes. Since pure A_1(LO) phonon modes can only be excited parallel to the z direction, the drastic reduction in intensity can be explained taking the directional phonon dispersion[3] into account. If the crystal is tilted, these modes gradually disappear. According to the dispersion picture of YANG et al.[3] they are extraordinary phonons, which change their character depending on the crystal axis tilt. Accordingly, A_1(TO) modes, which propagate perpendicular to the z axis, are enhanced under this scattering geometry, which explains the shift and intensity increase of the E(8TO) mode by the admixing of A_1(4TO).

---

[a] *Institut für Experimentelle Physik, Technische Universität Bergakademie Freiberg, Leipziger Str. 23, 09599 Freiberg, Germany. E-mail: thomas.koehler@physik.tu-freiberg.de, matthias.zschornak@physik.tu-freiberg.de*
[b] *Institut für Physik, Technische Universität Chemnitz, Reichenhainer Str. 70, 09126 Chemnitz, Germany.*
[c] *Institut Laue-Langevin, 71 Avenue des Martyrs, 38042 Grenoble, France.*
[d] *Institut für Angewandte Physik, Technische Universität Bergakademie Freiberg, Leipziger Str. 23, 09599 Freiberg, Germany.*

* Contributed equally to this work.

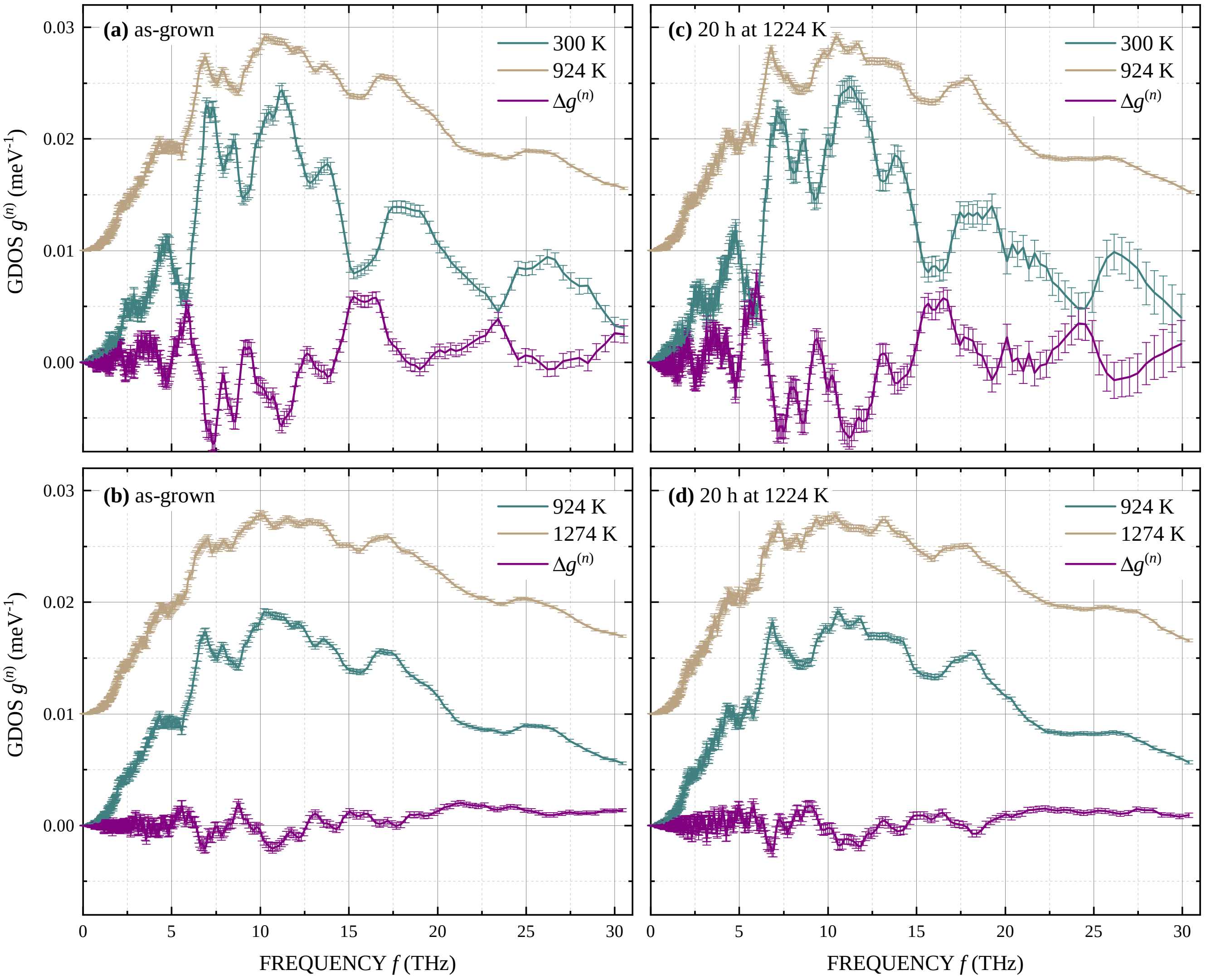

Fig. S1 *In situ* INS spectra of as-grown (a, b) and chemically reduced C-LiTaO$_3$ (c, d). For each temperature step, the difference curves $\Delta g^{(n)}$ (higher minus lower temperature) are shown. For optical clarity, the spectra are shifted from each other.

It can be clearly seen that the modes do not change further down to a depth of about 30 µm. This trend cannot be described by the macroscopic model of STONE et al.[2], since the domains are randomly arranged in the depolarised crystal. Thus, the scattering process on the walls occur at random angles. Moreover, it seems that some modes show a much more significant depth dependence than others. This indicates rather that the strain[4,5] between near-surface region and bulk changes, which affects the phonon modes differently.

Fig. S2 b shows the spectra recorded in $x(y, \mathrm{u})\bar{x}$ polarization configuration. In contrast to the spectra excited with the incident laser oriented parallel to the z direction, we find a shift of the E modes, that propagate in the x-y plane. Like the $x(z, \mathrm{u})\bar{x}$ geometry (see Fig. 6 b), this can only be explained by the strain in the material, since these modes do not have any frequency dependence on the angle according to the image of directional dispersion.

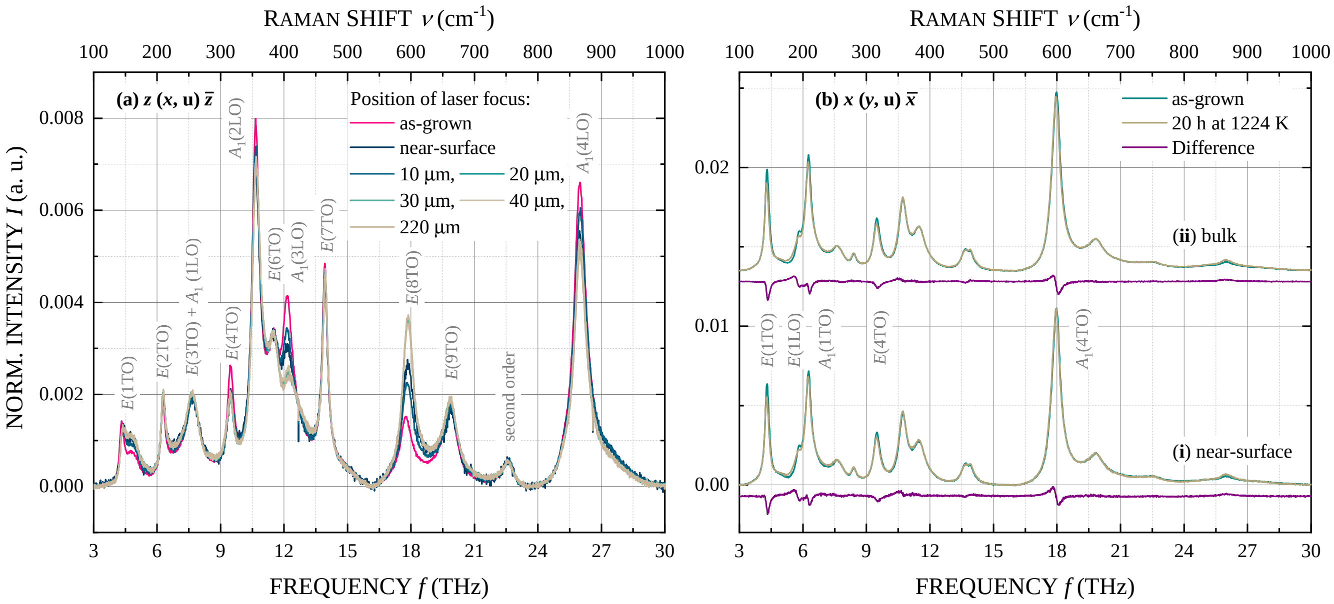

Fig. S2 (a) Raman spectra of chemically reduced C-LiTaO$_3$ in vacuum as a function of laser focus position recorded in $z(x,\mathrm{u})\bar{z}$ polarization configuration (the scattered light was not analysed (u); notation according to Porto[6] is used). (b) Raman spectra of as-grown and chemically reduced C-LiTaO$_3$ in vacuum for 20 h at 1224 K with focus on the near-surface region (i) and 30 µm into the material (ii) in $x(y,\mathrm{u})\bar{x}$ orientation. Only the changing phonon modes are labelled and for optical clarity, the spectra are shifted from each other.

S3 Determination of Li deficiency by FT-IR spectroscopy

Previous studies have shown that the OH$^-$ stretching vibration in the mid IR range can be used to estimate the Li concentration c_{Li} in the used melt. The OH$^-$ stretching vibration is strongly influenced by the intrinsic defect structure, the defect type and the concentration[7]. In the study of Bäumer et al.[8], different calibration crystals with varying Li$_2$O content in the melt composition were prepared and analysed with respect to the OH$^-$ band. Depending on the Li concentration, the OH$^-$ band shape, i.e. peak position, intensity and width, is influenced. This strong dependence of the OH$^-$ band on the defect concentration makes it a probe for the Li concentration. In the simplest case, the band can be fitted with a two sub-band model, although other descriptions exist[9]. The authors use a generalisation based on the intensity ratios $\alpha_{\nu,2}/\alpha_{\nu,1}$ of the two band components. The correlation from the present intensity ratios is:

$$c_{\mathrm{Li}} = 50\,\mathrm{mol\%} - 0.38\,\mathrm{mol\%} \cdot \sqrt{\alpha_{\nu,2}/\alpha_{\nu,1}}\,. \tag{1}$$

According to the proposed generalisation, we checked our crystals before powder preparation to estimate c_{Li} for their growth process. To fit the data, a two sub-band model is used by means of two pseudo-Voigt functions[7]. In Fig. S3, a value of $c_{\mathrm{Li}} = (48.74 \pm 0.22)$ mol% was obtained. This value is typical for the preparation of a congruent melting composition. However, the estimated value does not reflect the real Li deficit in the solid phase. During the growth process of C-LiTaO$_3$ there is an additional evaporation of Li$_2$O, so that the intrinsic Li deficit in the as-grown crystals is higher. This can be detected by INS in the solid phase and is consistent with previous data[10].

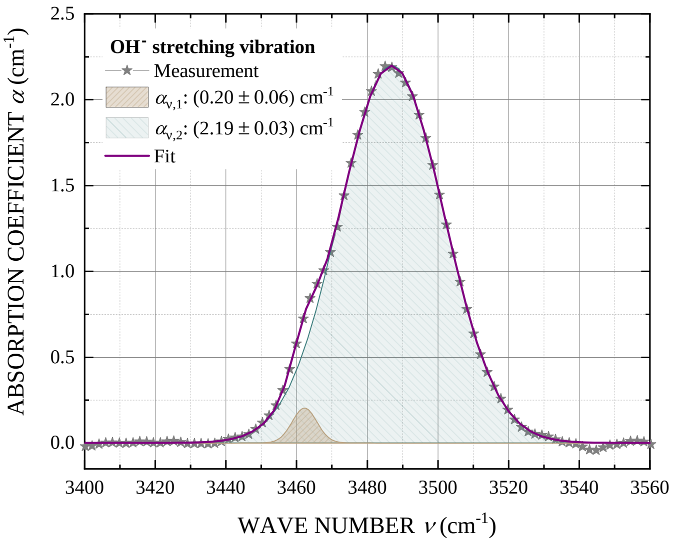

Fig. S3 OH^- absorption band of the as-grown crystals before milling to powder. The stretching vibration band is fitted with two pseudo-VOIGT profiles to determine the corresponding intensity ratio $\alpha_{v,2}/\alpha_{v,1}$.

S4 *Ex situ* powder investigations by X-ray diffraction

X-ray diffraction (XRD) patterns were recorded in reflective, symmetric, parallel beam geometry with Cu-$K\alpha_1$ ($\lambda = 1.540596$ Å) radiation on a $\theta - \theta$ goniometer (Bruker D8 Discover). The primary beam was parallelised and monochromatised using a GÖBEL mirror and an asymmetric Germanium 022 channel-cut monochromator. Furthermore, the primary beam was limited to a width of 0.1 mm. The axial divergence was limited to 2.5° in the secondary beam path, which was otherwise left open to take advantage of a position sensitive detector. Powder patterns were recorded for $2\theta = 15° \ldots 95°$ at a step-with of 0.01° with at least 60 s exposure time per point and continuous sample rotation at two revolutions per minute. Crystallite sizes of the samples were determined with Bruker Topas[11,12] after a calibration of the instrumental broadening of reflection profiles with NIST SRM640d silicon powder.

The powder patterns of the as-grown and reduced powder show phase pure (details below) lithium tantalate (fitted with the structure model of OHGAKI, ICSD collection code 84226[13]). The fits converge to rather bad R_{wp} values of approx. 15 %, which is due to *i*) the too large particle sizes and *ii*) the very strong preferred orientation of the particles along the cleavage plane $\{01\bar{1}2\}$ that is insufficiently modelleld with a MARCH-DOLLASE ansatz. While this does not impede impurity phase identification, it hinders structure refinement of the lithium tantalate. The XRD data of the chemically reduced C-$LiTaO_3$ powder are shown in Fig. S4. Our XRD data do not give any evidence for the existence of another phase besides C-$LiTaO_3$. Although it has been reported in the past that Li_2O is separated on thermally reduced C-$LiNbO_3$ powders[14], this cannot be identified in our data. If a crystalline phase in a sample is not detectable in a powder XRD measurement, two main reasons need to be considered: 1) the molar fraction of the phase is very small, say 1 mol% and 2) the crystallite size of the phase is so small that the BRAGG reflections become very broad and indistinguishable from the background. We have presented two scenarios in Fig. S4 b, that describe the lower limit for the measurability of Li_2O. The scenarios for Li_2O and Ta_2O_5 are shown under the assumption of a stoichiometric phase separation. Both models are overlaid with the XRD measurement of C-$LiTaO_3$ and the RIETVELD analysis is based on impurity phase concentrations of 4.2 mol%, which corresponds to 1.50 wt% and 3.78 wt% for Li_2O and Ta_2O_5, respectively with a grain size of 50 nm.

In Fig. S4 b it is noticeable that a concentration of 4.2 mol% Li_2O up to a grain size of 50 nm cannot be identified in the diffraction pattern. The χ^2 value of the RIETVELD analysis for C-$LiTaO_3$[13] is not significantly influenced by the presence of the Li_2O phase. Only above 50 nm crystallite size the reflections of Li_2O become distinguishable from the background. However, if a stoichiometric decomposition of C-$LiTaO_3$ were present, it should be possible to clearly identify Ta_2O_5 at the surface at the same concentration and grain size. However, this is not the case and together with the INS data it is obvious that no stoichiometric decomposition of C-$LiTaO_3$ can be observed. The presented data correspond to the interpretations of KAMINOV et al.[15], who studied annealed C-$LiNbO_3$ crystals, stating that a diffusion of NbO_2 or Nb_2O_5 to the surface is not expected, because the vapor pressure of pure NbO_2 is only 10^{-5} the value of pure Li_2O. We think that our data show a similar picture and that no Ta_xO_y phases should be expected. From comparable investigations on C-$LiNbO_3$ powders[14] it was shown that the powder samples can have a thin shell < 3 nm of Li_2O. As shown in our scenario, these thin shells are not accessible by powder diffraction.

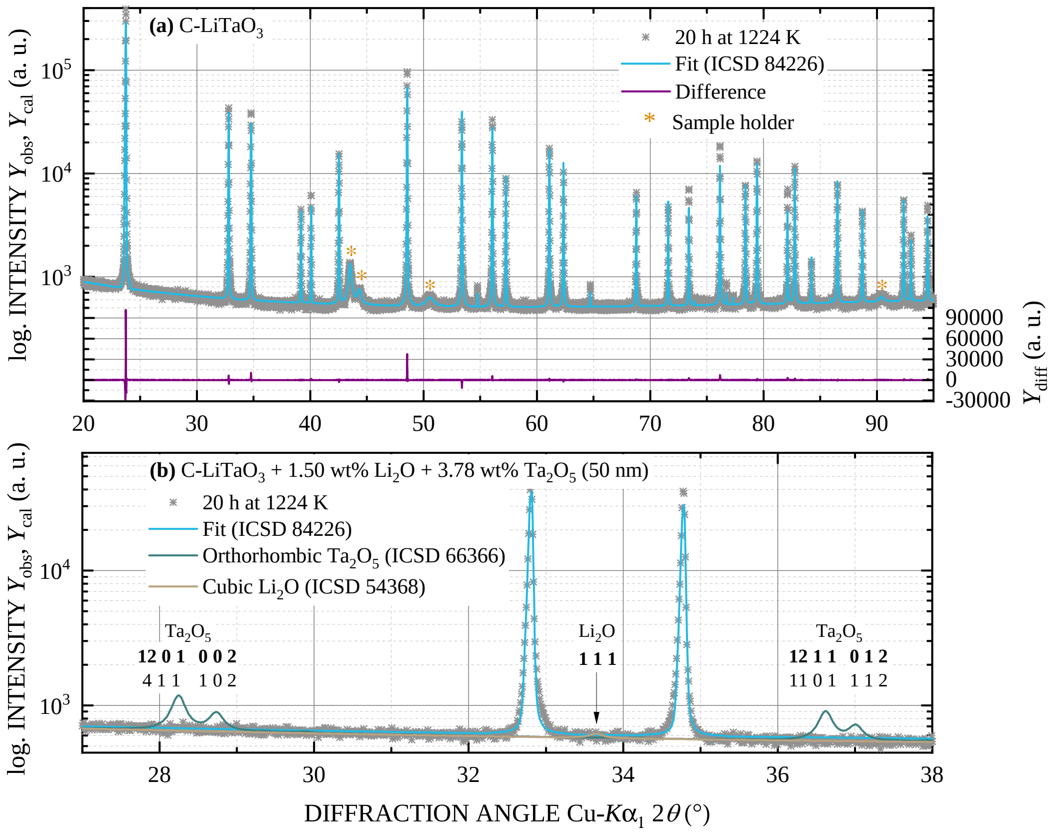

Fig. S4 XRD pattern of chemically reduced C-LiTaO$_3$ powder after neutron scattering experiments. The C-LiTaO$_3$ is fitted with the structure solution of OHGAKI et al.[13] (a). In addition, an amount of 4.2 mol% of Li$_2$O (a) and Ta$_2$O$_5$ has been assumed with a crystallite size of 50 nm (b). The dominant reflections of the Ta$_2$O$_5$ and Li$_2$O phases are marked with bold characters.

S5 *Ex situ* powder investigations by scanning electron microscopy

Surface examinations of C-LiTaO$_3$ powders were carried out using a scanning electron microscope (SEM) Helios NanoLab 600i from FEI. The images were taken at an acceleration voltage of 1 kV and a current of 43 pA using a secondary electron detector (TLD-SE). As-grown C-LiTaO$_3$ powder and annealed samples after INS measurement are examined *ex situ*. The oxidic samples are coated with 10 nm platinum via sputtering to reduce charging effects.

The SEM images show that the powdered as-grown C-LiTaO$_3$ grains have a size in the range of 63 … 40 µm, with homogeneously distributed C-LiTaO$_3$ nanoparticles ($\ll 1$ µm) on all grain surfaces (see Fig. S5 a). In addition, the particles show sharp step-like fractures, which are presumably caused by the individual fracture processes along cleavage plane $\{01\bar{1}2\}$ during milling. The as-grown single crystal powder samples do not show any noticeable features. It should be noted that the differences in brightness are due to charging effects of the oxidic samples, caused by incomplete metallization or missing contact to coated particles, and do not describe different phase regions of the material.

In contrast to the as-grown powder samples, the annealed material (see Fig. S5 b) shows a clearly modified surface. Previously sharp breaking edges and steps are rounded and appear much softer. A special feature are small faceted “pyramids” on all grain surfaces (see inset of Fig. S5 b). These grow out of the surface for up to 250 … 300 nm with a lateral extension up to ~ 500 nm. It is noticeable that most of these pyramids have a small sphere at the top. A possible explanation could be that the C-LiTaO$_3$ undergoes a kind of recrystallization process due to the thermal treatment. Driving force could be the minimization of the interfacial energy, caused by the misorientation between the grain and the support. Accelerated diffusion, especially in the neck between crumb and support can minimize the interfacial energy, explaining the faceted diffusion necks and rounded corners. Especially the small particles on the surface of the as-grown material show this behaviour. It seems that the smallest particles are preferred for this process by kinetic or energetic reasons.

In comparison, the surface of the chemically reduced single crystal (see Fig. S5 c) shows round outbreaks and microcracks on the surface. Such phenomena on single crystals have been described in the past with the strain of the material and a stoichiometry gradient at the surface[16]. It can be assumed that a movement of intrinsic/extrinsic lattice defects in the material towards the surface is thermally activated, which cluster at the surface and manifest in corresponding circular shaped objects.

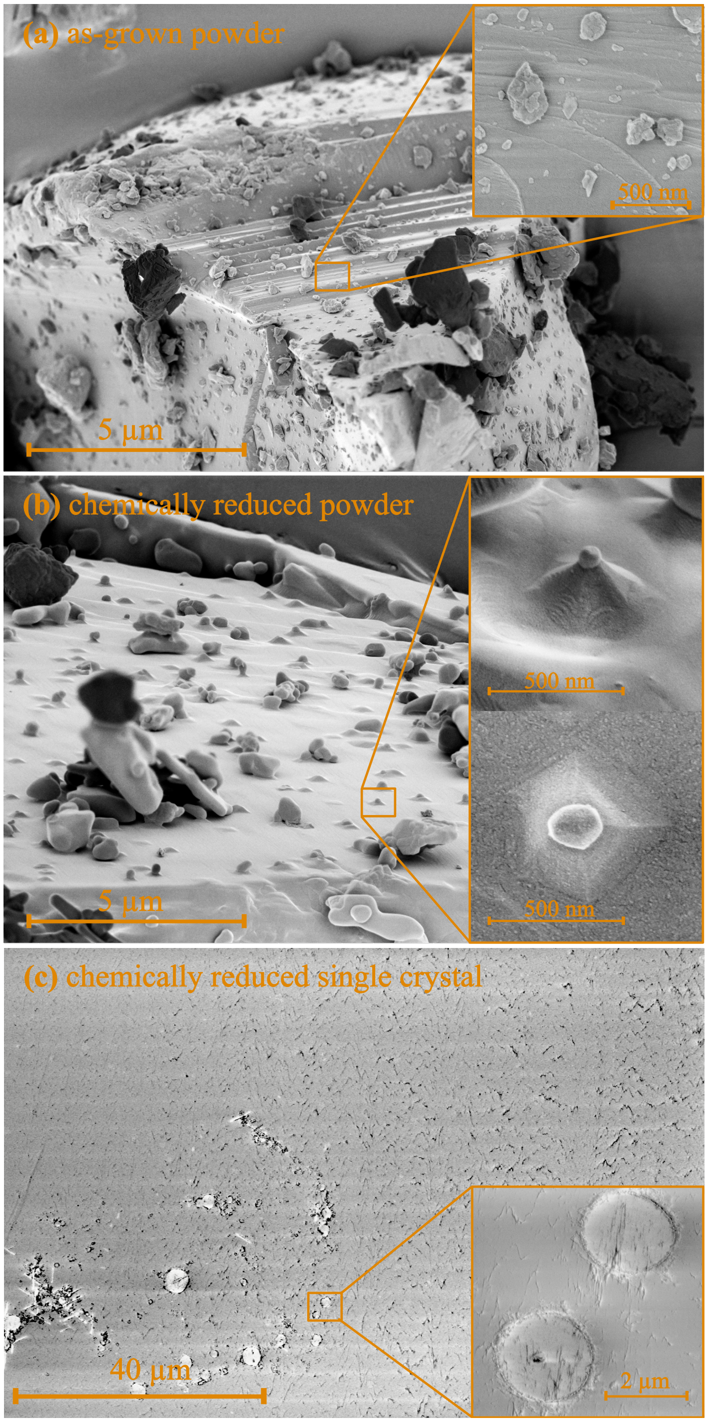

Fig. S5 SEM analysis on as-grown C-LiTaO_3 powder (a), chemically reduced crystal powder (b) and chemically reduced single crystal (c). The thermal treatment leads to significant surface changes by presumably recrystallisation process. The powders in (a) and (b) were used for INS and in (c) the crystal was treated comparably at 1224 K for 20 h.

Notes and references

1 M. K. Gupta, B. Singh, P. Goel, R. Mittal, S. Rols and S. L. Chaplot, Physical Review B, 2019, **99**, 224304.

2 G. Stone and V. Dierolf, Optics Letters, 2012, **37**, 1032–1034.

3 X. Yang, G. Lan, B. Li and H. Wang, physica status solidi (b), 1987, **142**, 287–300.

4 M. Fontana, R. Hammoum, P. Bourson, S. Margueron and V. Y. Shur, Ferroelectrics, 2008, **373**, 26–31.

5 M. Rüsing, S. Neufeld, J. Brockmeier, C. Eigner, P. Mackwitz, K. Spychala, C. Silberhorn, W. G. Schmidt, G. Berth, A. Zrenner and S. Sanna, Physical Review Materials, 2018, **2**, 103801.

6 T. C. Damen, S. Porto and B. Tell, Physical Review, 1966, **142**, 570.

7 T. Köhler, E. Mehner, J. Hanzig, G. Gärtner, H. Stöcker, T. Leisegang and D. C. Meyer, Journal of Solid State Chemistry, 2016, **244**, 108–115.

8 C. Bäumer, C. David, K. Betzler, H. Hesse, K. Lengyel, L. Kovács and M. Wöhlecke, physica status solidi (a), 2004, **201**, R13–R16.

9 L. Shi, W. Yan and Y. Kong, The European Physical Journal Applied Physics, 2007, **40**, 77–81.

10 P. Bordui, R. Norwood, C. Bird and J. Carella, Journal of Applied Physics, 1995, **78**, 4647–4650.

11 Topas, General Profile and Structure Analysis Software for Powder Diffraction Data V5, Bruker AXS GmbH, Karlsruhe, Germany, 2014.

12 R. W. Cheary and A. Coelho, Journal of Applied Crystallography, 1992, **25**, 109–121.

13 M. Ohgaki, K. Tanaka and F. Marumo, Mineralogical Journal, 1989, **14**, 373–382.

14 L. Kocsor, L. Péter, G. Corradi, Z. Kis, J. Gubicza and L. Kovács, Crystals, 2019, **9**, 334.

15 I. Kaminow and J. Carruthers, Applied Physics Letters, 1973, **22**, 326–328.

16 J. Carruthers, I. Kaminow and L. Stulz, Applied Optics, 1974, **13**, 2333–2342.